Progress In Electromagnetics Research, Vol. 142, 505–521, 2013

EXTENDED HIGH RESOLUTION RANGE PROFILE-JET ENGINE MODULATION ANALYSIS WITH SIGNAL ECCENTRICITY

Ji Hoon Park[1, *], Woo Yong Yang[1], Jun Woo Bae[2], Seong Cheol Kang[2], and Noh Hoon Myung[1]

[1]Department of Electrical Engineering, Korea Advanced Institute of Science and Technology (KAIST), 335 Gwahangno, Yuseong-gu, Daejeon 305-701, Korea

[2]Samsung Thales, Sampyong-Dong, Bundang-Gu, Seongnam 463-400, Korea

Abstract—In this paper, high resolution range profile-jet engine modulation (HRRP-JEM) analysis is extended by including quantitative estimation of the jet engine location and extraction of the JEM micro-Doppler component. Based on a parametric model of the range cell data, signal eccentricity was introduced for the purpose of determining the jet engine location. Then, complex empirical mode decomposition (CEMD) was employed to extract the embedded JEM component. The signal eccentricity also served as an auxiliary means of CEMD-based micro-Doppler extraction. Application to the simulated HRRP-JEM data demonstrated that the analysis results described in this paper could be useful for advanced radar target recognition with HRRP-JEM.

1. INTRODUCTION

Inverse synthetic aperture radar (ISAR) imaging [1–4] has been widely employed as a representative radar target recognition method. However, for a few types of radar targets, the ISAR image may be limited by its cross-range dimension, which totally depends on the relative target rotation. Recently, the concept of high resolution range profile in conjunction with jet engine modulation (HRRP-JEM) for aircraft targets with jet engines was introduced [5, 6] as another radar

Received 1 August 2013, Accepted 12 September 2013, Scheduled 16 September 2013

* Corresponding author: Ji Hoon Park (dydynoel@kaist.ac.kr).

imaging method for target recognition. HRRP-JEM, also known as the combined HRR-JEM, uses a radar waveform with both high range resolution and high frequency resolution. By high range resolution, the information on the aircraft structure can be obtained from the HRRP. With high frequency resolution, the JEM [6–11], one of the micro-Doppler phenomena induced by a rotating jet engine compressor, can show its unique spectrum affected by several characteristics of the jet engine. Thus, an HRRP-JEM image composed of range and frequency axes is considered as an independent means for radar target recognition by localizing the equipped jet engine installed on the aircraft [5, 6, 12]. However, most literature dealing with radar imaging has not placed great emphasis on HRRP-JEM analysis.

In our previous work [12], an algorithm for automatically determining the jet engine location was proposed and basically postulated that after eliminating frequency components around the zero-frequency, the range cell related to the jet engine location had higher amplitude than other cells by the remaining 1st chopping harmonic of the JEM spectrum [10, 11]. However, this non-parametric approach does not consider the inherent signal characteristics, and ambiguity can arise from the threshold for discriminating the frequency range to be removed. Hence, this work should be extended by focusing on more quantitative analysis. In addition, the JEM component containing jet engine features needs to be further extracted for enhanced target recognition.

With a simple parametric model of the range cell data, this paper employs signal eccentricity [13–15] to quantitatively determine the jet engine location. For a limited dwell time, the eccentricity is expected to be useful for measuring the micro-Doppler contribution of each range cell. Then, we adopt complex empirical mode decomposition (CEMD) [16–20] to further extract the JEM component. Apart from existing criteria, the eccentricity also serves as a supplementary means for the CEMD-based micro-Doppler extraction. The rest of the paper is organized as follows: In Section 2, we briefly introduce the range cell data model and propose basic techniques for extended HRRP-JEM analysis. In Section 3, we examine the HRRP-JEM data obtained from virtual aircraft framework (VIRAF, by IDS inc.) simulations of realistic aircraft models. Finally, conclusions and future work are discussed in Section 4.

2. BASIC TECHNIQUES FOR EXTENDED HRRP-JEM ANALYSIS

2.1. Simple Parametric Model of Radar Cell Data

The signal in the range cell of the HRRP-JEM image is modelled on the basis of point scatterers [17, 21–23] and the problem geometry with related parameters is shown in Fig. 1. Q and P are the scattering points on the target with bulk rotation angle, $\theta(t)$ and on the rotating subordinate part, respectively. After the range tracking and the translational motion compensation, the radar received signal from Q with a wavelength of λ is given by

$$\begin{aligned} s_Q(t) &\approx \exp\left[j\frac{4\pi R_Q}{\lambda}\sin\theta(t)\right] = \exp\left[j\frac{4\pi R_Q}{\lambda}\sin(\omega_Q t+\theta_Q)\right] \\ &\approx \exp\left[j\frac{4\pi R_Q}{\lambda}\omega_Q t\right] \end{aligned} \tag{1}$$

where ω_Q denotes the angular frequency, and R_Q is the distance between the target geometrical center O and Q. After ignoring the initial angle θ_Q, $s_Q(t)$ becomes the form of linear phase modulation by the small accumulation angle assumption, namely $\omega_Q t \ll 1$. Hence, the instantaneous frequency of Q is time-invariant. The radar signal from P is represented by the sinusoidal phase modulation such that

$$s_P(t) = \exp\left[j\frac{4\pi R_P}{\lambda}\sin(\omega_P t)\right] \tag{2}$$

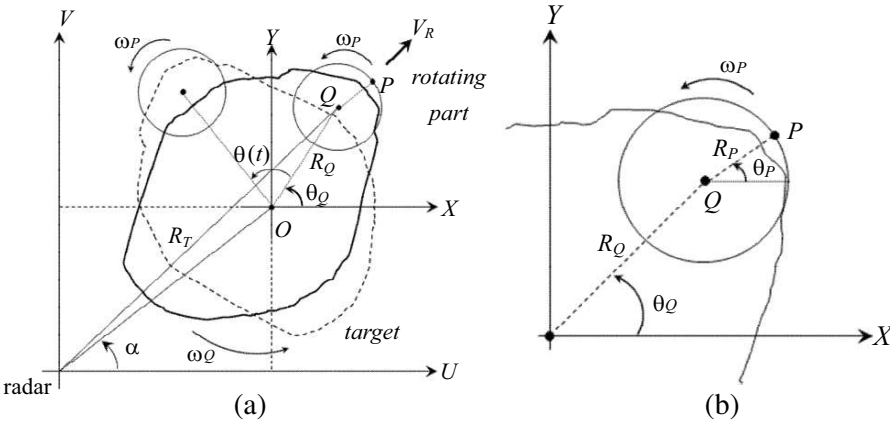

Figure 1. (a) Problem geometry of a target with a rotating part. (b) Expanded figure with respect to Q.

where ω_P is the angular speed of the rotating part and R_P the rotation radius. Note that the small accumulation angle assumption is not valid here since $\omega_P t$ is not generally small in relation to 1 [17, 23] and ω_P is much greater than ω_Q in the HRRP-JEM imaging scenario ($\omega_Q \ll \omega_P$). Consequently, the range cell data can be expressed by the sum of the body returned component $s_Q(t)$ and the micro-Doppler component $s_P(t)$ as follows:

$$s(t) = s_P(t) + A s_Q(t) = \exp\left[j\frac{4\pi R_P}{\lambda}\sin(\omega_P t)\right] + A\exp\left[j\frac{4\pi R_Q}{\lambda}\omega_Q t\right] \quad (3)$$

where A is the weight that makes the body returned component account for a relatively large portion of $s(t)$. This is because $s_P(t)$ may become weaker than $s_Q(t)$ if there is emphatic scattering from aircraft structures.

2.2. Signal Eccentricity and Its Application to Estimating Jet Engine Location

Signal eccentricity ε measures how far a complex-valued signal deviates from circularity with respect to the central axis of the complex plane [13–15]. By definition, it is expressed by main and minor axes of elliptical geometry when the signal $s(t) = \mathbf{s}$ is projected onto the 2D complex plane. However, since deterministically calculating the lengths of these axes is not always possible for an arbitrary data set, we use another mathematical expression based on the statistical characteristic of $\mathbf{s}$ such that [15]

$$\varepsilon = \sqrt{\left|\frac{P}{C}\right|} = \sqrt{\left|\frac{E\left[\mathbf{s}\cdot\mathbf{s}^T\right]}{E\left[\mathbf{s}\cdot\mathbf{s}^H\right]}\right|} \quad (4)$$

where P is the pseudo-covariance, C the covariance, and $E[\cdot]$ the expectation operator.

The eccentricity ranges between 0 for pure circular polarization and 1 for pure linear polarization. In (3), both signal components theoretically have 0 eccentricity values because they all have circularly rotating natures in the 3D complex domain composed of real, imaginary and time axes. However, in reality, the eccentricity cannot be 0 since the dwell time for radar imaging is within tens of milliseconds [6, 12, 17]. Thus, it can be highly dependent on the signal rotating behavior in the given dwell time. Since the body returned component $s_Q(t)$ slowly rotates compared to the micro-Doppler $s_P(t)$ ($\omega_Q \ll \omega_P$) [5, 6, 12], $s_Q(t)$ will appear to be linearly polarized as shown in Fig. 2(a) as opposed to $s_P(t)$, which will retain its circularity along the central axis of the complex plane as shown in Fig. 2(b). Table 1

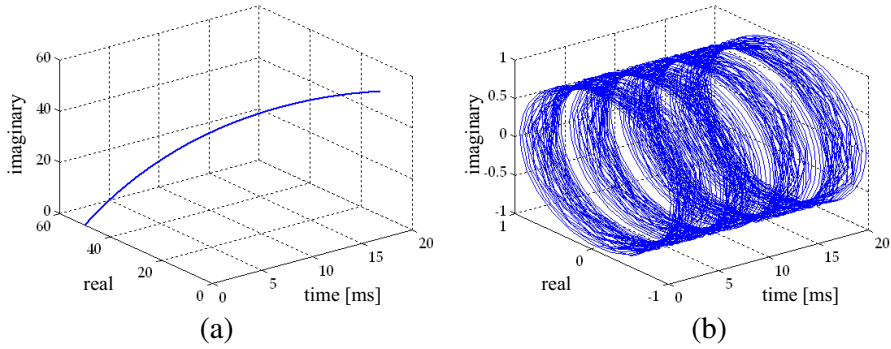

Figure 2. Signal rotating behavior for a dwell time of 20 ms. (a) $s_Q(t)$. (b) $s_P(t)$.

Table 1. Parameters of signal components depicted in Fig. 2.

parameters		value
radar wavelength λ		0.03 m
sampling frequency		80 kHz
dwell time		20 ms
parameters related to P and Q	R_P, ω_P	0.25 m, 200π rad/s
	R_Q, ω_Q, A	5.0 m, 0.05 rad/s, 50

gives background information on the signal components illustrated in Fig. 2. The large value of ω_P considers a scattering point on a propeller blade rotating at a rate of 6000 RPM.

Figure 3 shows eccentricity values of $s(t)$ for different A. If A is less than 1, the micro-Doppler contribution becomes dominant and $s(t)$ has a low eccentricity value. However, when A increases, the rotating behavior of $s(t)$ starts to deviate from circularity with respect to the central axis of the complex plane. Therefore, the signal eccentricity is feasible for assessing the micro-Doppler contribution to the range cell data. To further develop our discussion on localization of the jet engine, the eccentricity concept will be applied to HRRP-JEM images. Since the JEM micro-Doppler contribution will be maximized at the engine location, the corresponding range cell is expected to be found by investigating the eccentricity of each range cell.

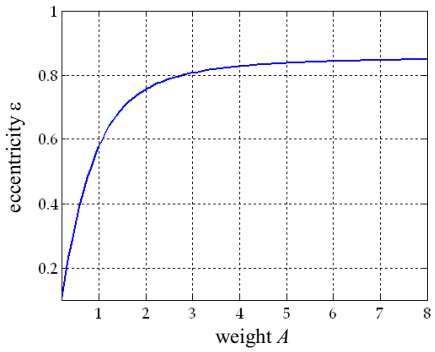

Figure 3. Eccentricity values of $s(t)$ by changing A.

2.3. Micro-Doppler Extraction via CEMD Incorporated with Signal Eccentricity

Once the range cell indicating the jet engine location is found, the JEM component can be further extracted from the range cell data, which still contains the body returned component. In this paper, we adopt CEMD [16], an extension of real-valued EMD [24], as an extraction method. Its underlying idea is to regard the complex-valued signal as rapidly rotating components superimposed on slowly rotating components. Thus, CEMD successively separates zero-mean rotating components from the original signal by projecting it in uniformly spaced directions along a unit circle. Each decomposed component is referred to as the complex intrinsic mode function (IMF). Since CEMD has fully data-driven characteristics, namely, it makes no prior assumption on the given data, many researchers have demonstrated its effectiveness in a variety of applications [17–20]. Since the detailed algorithm has been presented in many papers, we will not repeat it here to keep this paper concise.

We use (3) again to illustrate the CEMD-based micro-Doppler extraction. A is given as 50 to imitate the range cell data in which the body returned component strongly overlaps with the micro-Doppler. The CEMD with 127 projection directions is applied to $s(t)$ and 3 complex IMFs are obtained. Since the micro-Doppler can be reconstructed by combining appropriate IMFs, a standard for IMF selection needs to be set up. In [17], Bai et al. proposed the number of zero-crossings as a standard for IMF discrimination to separate the micro-Doppler from the body Doppler in ISAR imaging. It can be a physically intuitive means because it basically assumes that the micro-Doppler varies much more rapidly than the body Doppler. However,

the zero-crossing threshold may not be clear if there is no rapid change in the number of zero-crossings. Furthermore, in contrast to our situation dealing with the HRRP-JEM data, the micro-Doppler discussed in [17] accounts for a substantial portion of the range cell data. Therefore, we propose the eccentricity as a new complementary means to consider the rotating behavior of the reconstructed signal.

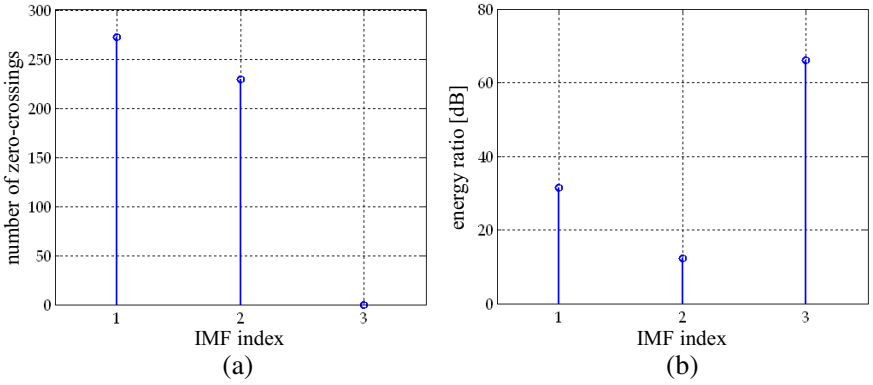

Figure 4. Investigation into 3 extracted IMFs. (a) Numbers of zero-crossings. (b) Energy ratio in a dB scale.

Figure 4 shows the number of zero-crossings and the energy ratio of each extracted IMF. The first two IMFs have numerous zero-crossings while their energy values are at least 30 dB lower than that of the 3rd IMF. Thus, it can be anticipated that these IMFs contain the micro-Doppler component. To clarify this observation, we then calculate the eccentricity for IMF combinations: $r_1(t)$, $r_2(t)$ and $r_3(t)$. Here, $r_n(t)$ is given by

$$r_n(t) = \sum_{i=1}^{n} c_i(t) \tag{5}$$

where $c_i(t)$ is the ith IMF, and IMFs are combined by the ascending order in accordance with the degree of rotation. Note that $r_n(t)$ becomes identical with the original signal when n is equal to the number of extracted IMFs. The eccentricity of each $r_n(t)$ is 0.1576, 0.1099 and 0.8577, respectively. The eccentricity value of $r_3(t)$ quantitatively reveals that the last IMF denotes the body returned component as predicted from Fig. 4. After separating the 3rd IMF, $r_2(t)$ with the minimum eccentricity is regarded as best characterizing the micro-Doppler component and is designated as the reconstructed micro-Doppler component. Since the 2nd IMF has relatively low

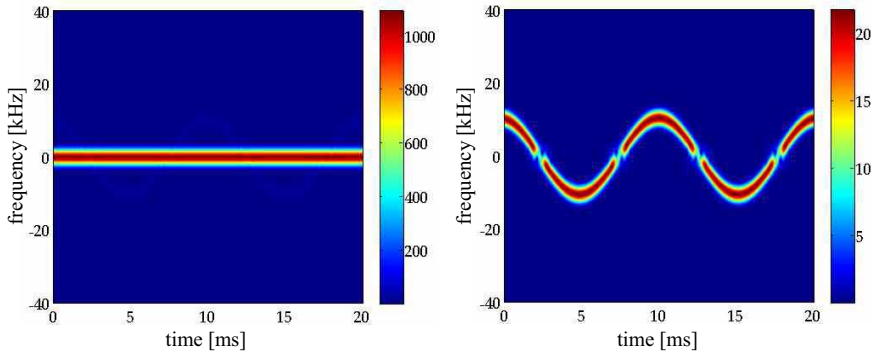

Figure 5. Spectrograms related to micro-Doppler extraction. (a) $s(t)$. (b) $r_2(t)$.

energy, $r_1(t)$ is allowed to be selected despite its relatively high eccentricity. Therefore, the signal eccentricity does not severely restrict the IMFs to be used but indicates the desirable IMF combination.

Figure 5 presents the spectrograms of $s(t)$ and $r_2(t)$. Even though Fig. 5(a) exhibits an almost constant frequency line, Fig. 5(b) depicts a time-dependent frequency and shows quite a good match with the theoretical micro-Doppler frequency, which can be derived from the phase term in (2) as follows:

$$f(t) = \frac{1}{2\pi}\frac{d}{dt}\left[\frac{4\pi R_P}{\lambda}\sin(\omega_P t)\right] = \frac{2}{\lambda}R_P\omega_P\cos(\omega_P t) \tag{6}$$

3. APPLICATION OF PROPOSED TECHNIQUES TO HRRP-JEM IMAGES

3.1. Estimation of Jet Engine Location

To verify the proposed techniques, this section examines the 2D RCS data set [12] obtained from VIRAF simulations of two realistic aircraft models. These aircraft models are equipped with jet engines as shown in Fig. 6 and were assumed to be stationary for typical HRRP-JEM images without cross-range dimensions. Table 2 gives electromagnetic simulation parameters and relevant geometrical and dynamic characteristics.

Figure 7 shows Fourier-based HRRP-JEM images of the aircraft models. In the Global Hawk, the head and tail positions can be observed at the 4th and 18th range cells in accordance with the

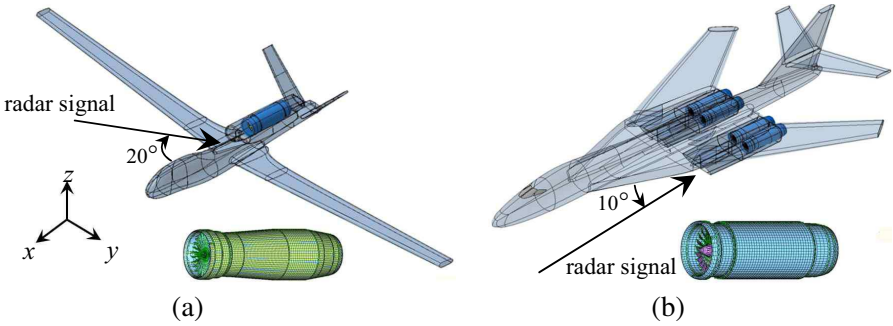

Figure 6. Simulated aircraft models equipped with jet engine models. (a) Global Hawk and AE3007 engine. (b) B-1B Bomber and F101 engines.

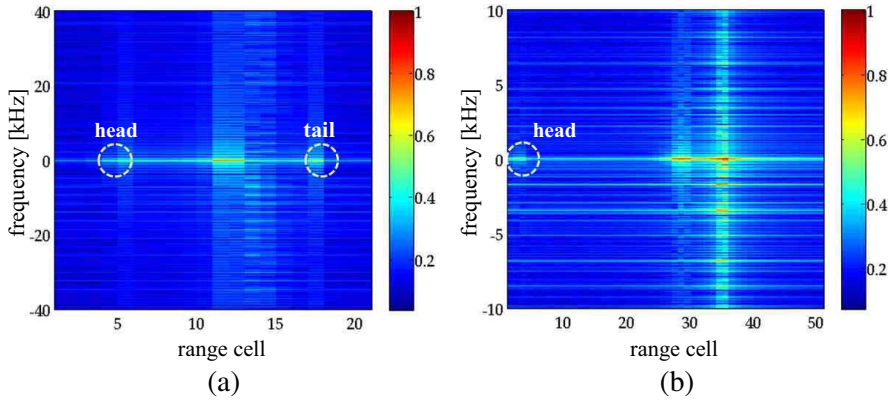

Figure 7. Fourier-based HRRP-JEM images of aircraft models. (a) Global Hawk. (b) B-1B Bomber.

projected length. In addition, broad spectra are shown at the 11th–14th range cells. Although these spectra suggest the existence of the JEM harmonic spectrum, it is difficult to determine the range cell indicating the actual jet engine location.

For discrimination accuracy, some range cells are excluded in the eccentricity computation when they do not overlap with the effective aircraft range or their maximum RCS values do not reach the predetermined small value of -20 dBsm as shown in Fig. 8(a). This is because the JEM-related spurious components existent throughout the ranges can also give a small eccentricity even if they do not have a real influence on the HRRP-JEM image. Fig. 8(b) exhibits the

Table 2. Electromagnetic simulation parameters for HRRP-JEM imaging and geometrical and dynamic characteristics of two aircraft models with jet engines.

	aircraft model	**Global Hawk**	**B-1B Bomber**
electromagnetic simulations	electromagnetic analysis method	shooting and bouncing rays (SBR) [25, 26]	
	radar center frequency	10 GHz	
	bandwidth	150 MHz (range resolution = 1 m)	
	frequency interval	7.5 MHz	3 MHz
	number of frequency steps	21	51
	pulse repetition frequency (PRF)	80 kHz	20 kHz
	dwell time	20 ms (frequency resolution = 50 Hz)	
	incident angle (azimuth $\Phi = 0°$)	70°	100°
characteristics of two aircraft models with jet engines	projected length by incident angle	13.34 m	47.96 m
	projected distance from head to engine	8.46 m	31.51 m
	number of equipped jet engines	1	4
	engine model	**AE3007**	**F101**
	full rotation speed	6000 RPM	
	number of blades in 1st rotor stage	23	17
	length of blades in 1st rotor stage	0.491 m	0.385 m

eccentricity values calculated for the rest of range cells, and the 13th range cell shows the lowest eccentricity. Since there are 9 cells between the head and the engine, the estimated range cell corresponds to the real location at which the distance to the head is 8.46 m. If the range resolution of 1 m is further improved by the wide bandwidth, more accurate localization can be performed. The eccentricity also confirms that the 11th and 12th range cells with high eccentricity denote the

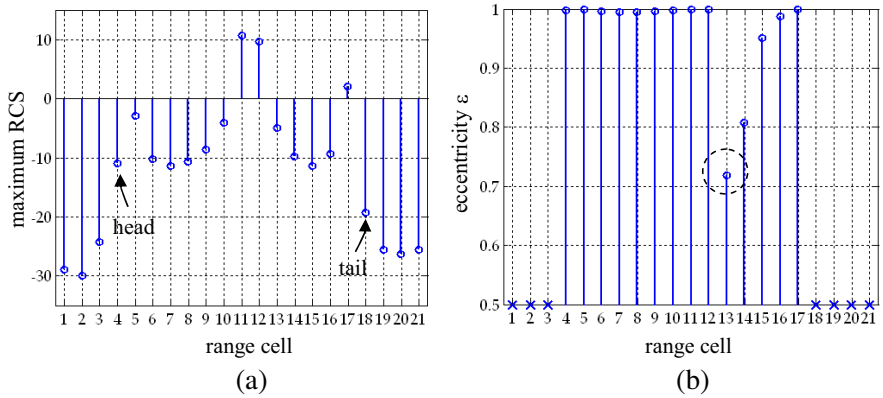

Figure 8. Characteristics of range cell data in the Global Hawk. (a) Maximum RCS. (b) Eccentricity.

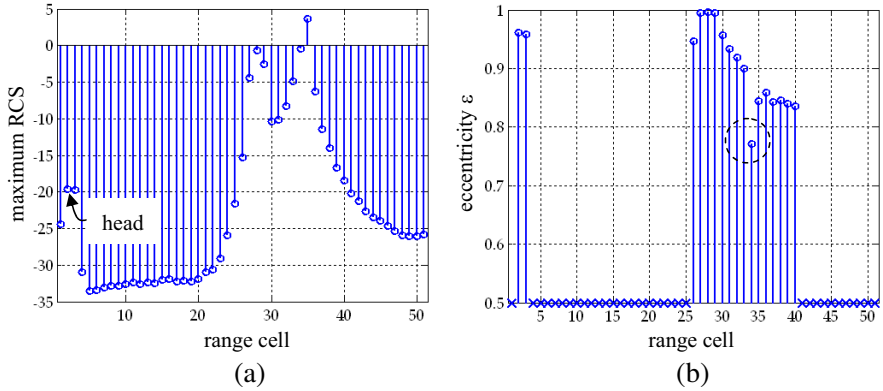

Figure 9. Characteristics of range cell data in the B-1B Bomber. (a) Maximum RCS. (b) Eccentricity.

scattering from the aircraft structure.

In the B-1B Bomber, the tail position is not clear, as depicted in Figs. 7(b) and 9(a). Thus, the jet engine location is estimated with respect to the head position at the 2nd range cell. Although there are two JEM-like broad spectra at the 27th–29th range cells and at the 34th–36th range cells, we cannot clearly conclude which range cell denotes the real jet engine location. Fig. 9(b) shows the eccentricity of the range cells with RCS values greater than -20 dBsm. It can be shown that the 34th range cell with the minimum eccentricity is identified as the jet engine location from which the distance to the head

is 31.51 m. Other JEM-like spectra at the 27th–29th range cells are shown to be mainly contributed to by the body returned component. This section demonstrated that the eccentricity could facilitate the quantitative estimation of the jet engine location.

3.2. Extraction of JEM Component

Figure 10(a) shows the spectrogram of the 13th range cell data in the Global Hawk. The spectrogram confirms that the strong body returned component still exists around the zero frequency. The CEMD with 127 directions decomposed the data into 9 IMFs, and their numbers of zero-crossings and the energy ratio are shown in Fig. 10(b). Although the number of zero-crossings of the 1st IMF is much more than the others, most of the energy lies in the 2nd IMF except for the 9th IMF, which obviously coincides with the strong zero-frequency component. Hence, it is not clear which IMF should be included for accurate JEM extraction. As evident from Table 3, the eccentricity values of

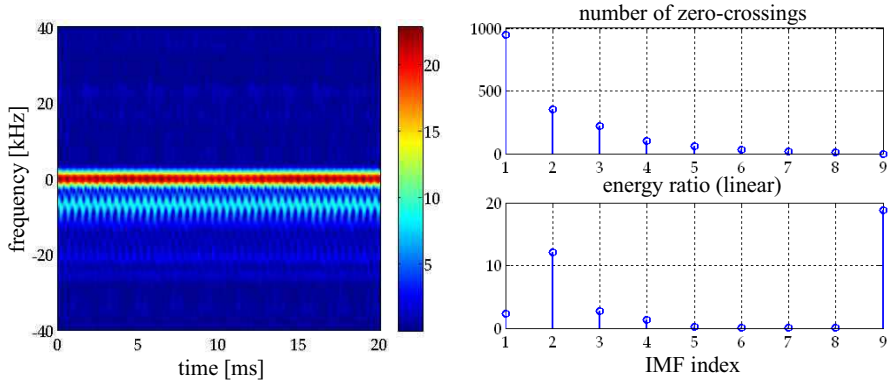

Figure 10. (a) Spectrogram of 13th range cell data in the Global Hawk. (b) Numbers of zero-crossings and the energy ratio of 9 extracted IMFs.

Table 3. Calculated eccentricity for IMF combinations of two aircraft cases.

	$r_1(t)$	$r_2(t)$	$r_3(t)$	$r_4(t)$	$r_5(t)$	$r_6(t)$	$r_7(t)$	$r_8(t)$	$r_9(t)$
Global Hawk	0.3513	0.3721	0.3262	0.3174	0.3149	0.3136	0.3135	0.3135	0.7193
B-1B Bomber	0.2820	0.4140	0.4667	0.4487	0.4355	0.4363	0.7711	–	–

reconstructed signals ($r_1(t) \sim r_8(t)$) do not sharply increase until the last 9th IMF is added. Based on the minimum eccentricity, $r_8(t)$ is selected as the extracted JEM component.

Figure 11 depicts the spectrogram of $r_8(t)$ where the JEM component is more concentrated than in the spectrogram of Fig. 10(a). From Fig. 11(b), we can obtain a variety of information, such as the chopping rate, the blade length, and the blade parity (whether the number of blades is even or odd). The chopping rate [6, 11], the period when a blade moves to its neighbor position, can be calculated as 0.435 ms. The blade length is estimated using the Doppler span [8, 10, 11] along the frequency axis. The slanted waveforms marked with white lines suggest the odd number of blades for which the blades alternately approach and recede [8].

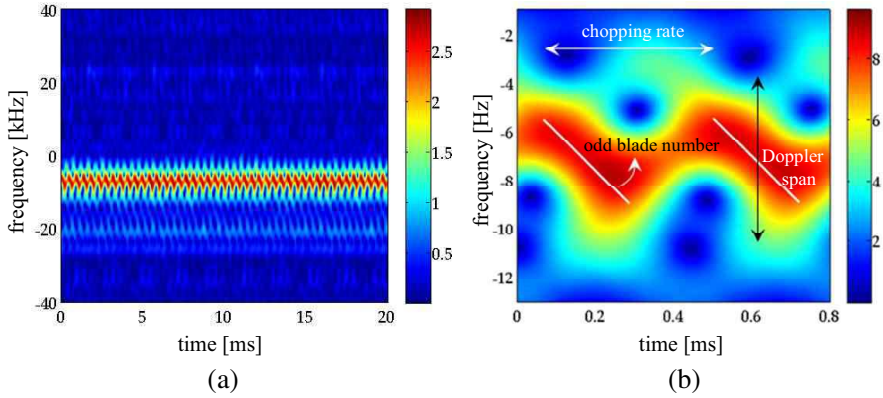

Figure 11. (a) Spectrogram of $r_8(t)$ in the Global Hawk. (b) Expanded spectrogram related to (a).

Figure 12(a) shows the spectrogram of the 34th range cell data in the B-1B Bomber. Although it presents the relatively strong micro-Doppler by simultaneous scattering from 4 engines, further processing is needed for more accurate JEM analysis. Table 3 supports that $r_1(t)$ is designated as the extracted JEM component. One remarkable characteristic of the auto-correlation of $r_1(t)$ shown in Fig. 12(b) is the spool rate (full rotation period), one of the typical JEM characteristics. The outstanding peaks associated with the spool rate exist among surrounding peaks related to the chopping rate. Thus, using the time intervals of the auto-correlation, the number of blades can be calculated as 17. From Figs. 12(c) and 12(d), it is noteworthy that the refined spectrogram of $r_1(t)$ exhibiting slanted lines leads to the more distinct even/odd check of the blade number than Fig. 12(a).

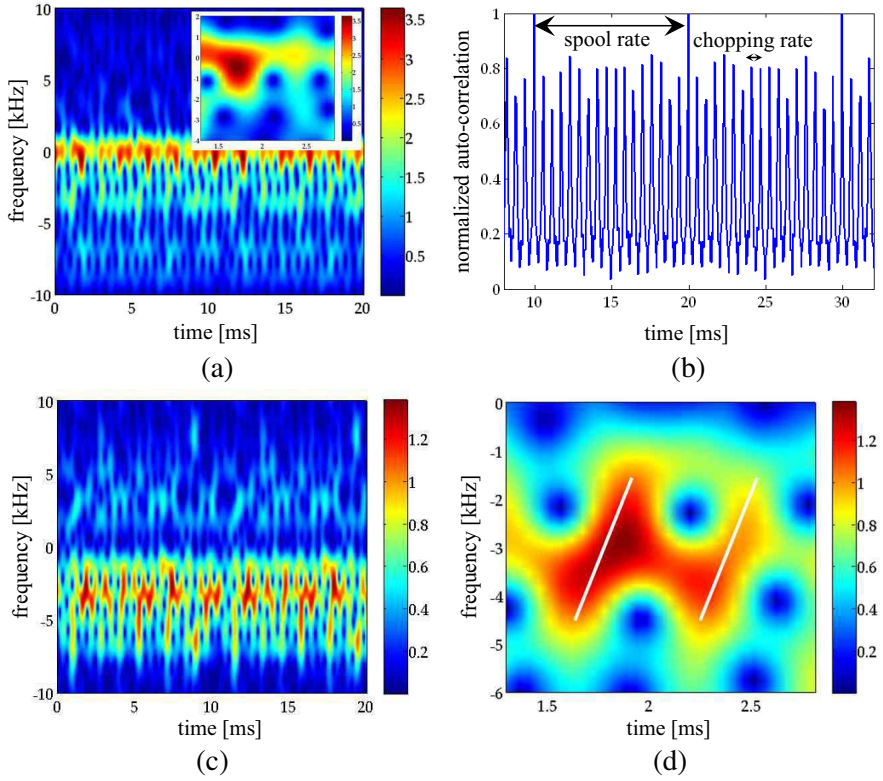

Figure 12. (a) Spectrogram of the 34th range cell data in the B-1B Bomber (expanded between 1.3 ms and 2.8 ms). (b) Unbiased auto-correlation of $r_1(t)$. (c) Spectrogram of $r_1(t)$. (d) Expanded spectrogram related to (c).

4. CONCLUSION

This paper presents an extended HRRP-JEM analysis with signal eccentricity: the estimation of the jet engine location and the extraction of the JEM component via CEMD. Based on the range cell data model, we employed the eccentricity as a metric for assessing the micro-Doppler contribution. Rather than the non-parametric approach, the signal eccentricity served as a reliable indicator by facilitating more quantitative jet engine localization. In addition, further application of eccentricity could provide a new supplementary means for the CEMD-based JEM extraction. Future studies should focus on examining the measured data where the clarity of HRRP-

JEM images would be degraded by the aircraft motion. To maintain the quality of HRRP-JEM images, not only the aircraft target but also the rotating jet engines need to be continuously tracked by the radar during the dwell time. Although this paper dealt with HRRP-JEM images with one JEM line, more than two jet engines can be illuminated by the radar signal and can be located at different range cells. Therefore, HRRP-JEM images with more than two JEM lines can also provide later research direction. However, the fundamental principles of this research can be followed because the eccentricity was proven to be effective for evaluating the micro-Doppler contribution. The extended HRRP-JEM analysis described in this paper is expected to be useful for advanced radar target recognition with HRRP-JEM.

ACKNOWLEDGMENT

This research was supported by Samsung Thales Co., Ltd..

REFERENCES

1. Park, S.-H., J.-H. Lee, and K.-T. Kim, "Performance analysis of the scenario-based construction method for real target ISAR recognition," *Progress In Electromagnetics Research*, Vol. 128, 137–151, 2012.
2. Calvo-Gallego, J. and F. Pérez-Martínez, "Simple traffic surveillance system based on range-Doppler radar images," *Progress In Electromagnetics Research*, Vol. 125, 343–364, 2012.
3. Felguera-Martin, D., J.-T. Gonzalez-Partida, and M. Burgos-Garcia, "Interferometric ISAR imaging on maritime target applications: Simulation of realistic targets and dynamics," *Progress In Electromagnetics Research*, Vol. 132, 571–586, 2012.
4. Park, J.-H. and N.-H. Myung, "Enhanced and efficient ISAR image focusing using the discrete Gabor representation in an oversampling scheme," *Progress In Electromagnetics Research*, Vol. 138, 227–244, 2013.
5. Tait, P., "Target classification for air defense radars," *IET Seminar on High Resolution Imaging and Target Classification*, 3–16, London, 2006.
6. Tait, P., *Introduction to Radar Target Recognition*, IET Radar, Sonar and Navigation Series 18, 2005.
7. Bell, M. R. and R. A. Grubbs, "JEM modeling and measurement for radar target identification," *IEEE Trans. on Aerospace and Electronic Systems*, Vol. 29, No. 1, 73–87, 1993.

8. Lim, H., J. H. Park, J. H. Yoo, C. H. Kim, K. I. Kwon, and N. H. Myung, "Joint time-frequency analysis of radar micro-Doppler signatures from aircraft engine models," *Journal of Electromagnetic Waves and Applications*, Vol. 25, Nos. 8–9, 1069–1080, 2011.
9. Lim, H., J. H. Yoo, C. H. Kim, K. I. Kwon, and N. H. Myung, "Radar cross section measurement of a realistic jet engine structure with rotating parts," *Journal of Electromagnetic Waves and Applications*, Vol. 25, No. 7, 999–108, 2011.
10. Park, J. H., H. Lim, and N. H. Myung, "Modified Hilbert-Huang transform and its application to measured micro Doppler signatures from realistic jet engine models," *Progress In Electromagnetics Research*, Vol. 126, 255–268, 2012.
11. Park, J. H., H. Lim, and N. H. Myung, "Analysis of jet engine modulation effect with extended Hilbert-Huang transform," *Electronics Letters*, Vol. 49, No. 3, 215–216, 2013.
12. Lim, H. and N. H. Myung, "High resolution range profile-jet engine modulation analysis of aircraft models," *Journal of Electromagnetic Waves and Applications*, Vol. 25, Nos. 8–9, 1092–1102, 2011.
13. Ollila, E., "On the circularity of a complex random variable," *IEEE Signal Processing Letters*, Vol. 15, 841–844, 2008.
14. Lilly, J. M. and S. C. Olhede, "Bivariate instantaneous frequency and bandwidth," *IEEE Trans. on Signal Processing*, Vol. 58, No. 2, 591–603, 2010.
15. Ahrabian, A., N. U. Rehman, and D. Mandic, "Bivariate empirical mode decomposition for unbalanced real-world signals," *IEEE Signal Processing Letters*, Vol. 20, No. 3, 245–248, 2013.
16. Rilling, G., P. Flandrin, P. Goncalves, and J. M. Lilly, "Bivariate empirical mode decomposition," *IEEE Signal Processing Letters*, Vol. 14, No. 12, 936–939, 2007.
17. Bai, X., M. Xing, F. Zhou, G. Lu, and Z. Bao, "Imaging of micromotion targets with rotating parts based on empirical mode decomposition," *IEEE Trans. on Geoscience and Remote Sensing*, Vol. 46, No. 11, 3514–3523, 2008.
18. Niu, J., Y. Liu, W. Jiang, X. Li, and G. Kuang, "Weighted average frequency algorithm for Hilbert-Huang spectrum and its application to micro-Doppler estimation," *IET Radar, Sonar and Navigation*, Vol. 6, No. 7, 595–602, 2011.
19. Zhou, F., M. Xing, X. Bai, G. Sun, and Z. Bao, "Narrow-band interference suppression for SAR based on complex empirical

mode decomposition," *IEEE Geoscience and Remote Sensing Letters*, Vol. 6, No. 3, 423–427, 2009.

20. Yang, W., R. Court, P. J. Tavner, and C. J. Crabtree, "Bivariate empirical mode decomposition and its contribution to wind turbine condition monitoring," *Journal of Sound and Vibration* Vol. 330, 3766–3782, 2011.
21. Li, P., D. Wang, and L. Wang, "Separation of micro-Doppler signals based on time frequency filter and Viterbi algorithm," *Image and Video Processing*, Vol. 7, No. 3, 593–605, 2011.
22. Stankovic, L., V. Popovic-Bugarin, and P. Radenovic, "Genetic algorithm for rigid body reconstruction after micro-Doppler removal in the radar imaging analysis," *Signal Processing*, Vol. 93, 1921–1932, 2013.
23. Stankovic, L., I. Djurovic, and T. Thayaparan, "Separation of target rigid body and micro-Doppler effects in ISAR imaging," *IEEE Trans. on Aerospace and Electronic Systems*, Vol. 42, No. 4, 1496–1506, 2006.
24. Huang, N. E., Z. Shen, S. R. Long, M. C. Wu, H. H. Shih, Q. Zheng, N. C. Yen, C. C. Tung, and H. H. Liu, "The empirical mode decomposition and the Hilbert spectrum for nonlinear and non-stationary time series analysis," *Proc. Royal. Society A*, Vol. 454, No. 1971, 679–699, 1998.
25. Gao, P. C., Y. B. Tao, Z. H. Bai, and H. Lin, "Mapping the SBR and TW-ILDCs to heterogeneous CPU-GPU architecture for fast computation of electromagnetic scattering," *Progress In Electromagnetics Research*, Vol. 122, 137–154, 2012.
26. Buddendic, H. and T. F. Eibert, "Bistatic image formation from shooting and bouncing rays simulated current distributions," *Progress In Electromagnetics Research*, Vol. 119, 1–18, 2011.